6. Rayleigh, Lord *The Theory of Sound* Vol. II 346–350 (Dover, New York, 1944).
7. Tan, J. & Gabrielse, G. Synchronization of parametrically pumped electron oscillators with phase bistability. *Phys. Rev. Lett.* **67,** 3090–3093 (1991).
8. Howson, D. P. & Smith, R. B. *Parametric Amplifiers* (McGraw-Hill, New York, 1970).
9. Likharev, K. K. *Dynamics of Josephson Junctions and Circuits* (Gordon & Breach Science, Philadelphia, 1986).
10. Levy, D. M. & Keller, J. B. Instability intervals of Hill's equation. *Commun. Pure Appl. Math.* **16,** 458–476 (1963).
11. Saif, M. T. A. & MacDonald, N. C. Measurement of forces and spring constants of microinstruments. *Rev. Sci. Instrum.* **69,** 1410–1422 (1998).
12. Miller, S. A., Turner, K. L. & MacDonald, N. C. Microelectromechanical scanning probe instruments for array architectures. *Rev. Sci. Instrum.* **68,** 4155–4162 (1997).
13. Timp, G. (ed.) *Nano-Science and Technology* (AIP, Woodbury, in the press).
14. Carr, W. N. (ed.) *J. Micromech. Microeng.* **4,** (4: special issue on microfluids) (1994).
15. Tang, W. C., Lim, M. G. & Howe, R. T. Electrostatic comb drive levitation and control method. *J. MicroElectroMechan. Syst.* **1,** 170–178 (1992).
16. COULOMB (Integrated Engineering Software, Inc., 1989).

Acknowledgements. We thank F. Bertsch for experimental assistance. This work was supported in part by the National Science Foundation and the Defense Advanced Research Projects Agency.

Correspondence and requests for materials should be addressed to K.L.T. (e-mail: turner@tam.cornell.edu).

Generalized syntheses of large-pore mesoporous metal oxides with semicrystalline frameworks

Peidong Yang*, Dongyuan Zhao*†, David I. Margolese*, Bradley F. Chmelka†‡ & Galen D. Stucky*†

* *Departments of Chemistry and Materials,* † *Materials Research Laboratory,* ‡ *Department of Chemical Engineering, University of California, Santa Barbara, California 93106, USA*

Surfactants have been shown to organize silica into a variety of mesoporous forms, through the mediation of electrostatic, hydrogen-bonding, covalent and van der Waals interactions[1–8]. This approach to mesostructured materials has been extended, with sporadic success, to non-silica oxides[5–17], which might promise applications involving electron transfer or magnetic interactions. Here we report a simple and versatile procedure for the synthesis of thermally stable, ordered, large-pore (up to 140 Å) mesoporous metal oxides, including TiO_2, ZrO_2, Al_2O_3, Nb_2O_5, Ta_2O_5, WO_3, HfO_2, SnO_2, and mixed oxides $SiAlO_{3.5}$, $SiTiO_4$, $ZrTiO_4$, Al_2TiO_5 and ZrW_2O_8. We used amphiphilic poly(alkylene oxide) block copolymers as structure-directing agents in non-aqueous solutions for organizing the network-forming metal-oxide species, for which inorganic salts serve as precursors. Whereas the pore walls of surfactant-templated mesoporous silica[1] are amorphous, our mesoporous oxides contain nanocrystalline domains within relatively thick amorphous walls. We believe that these materials are formed through a mechanism that combines block copolymer self-assembly with complexation of the inorganic species.

In a typical synthesis, 1 g of poly(alkylene oxide) block copolymer $HO(CH_2CH_2O)_{20}(CH_2CH(CH_3)O)_{70}(CH_2CH_2O)_{20}H$ (designated $EO_{20}PO_{70}EO_{20}$; Pluronic P-123, BASF) was dissolved in 10 g of ethanol (EtOH). To this solution, 0.01 mol of the respective inorganic chloride precursor (Table 1) was added with vigorous stirring for 1/2 h. The resulting sol solution was gelled in an open Petri dish at 40 °C in air for 1–7 days, during which the inorganic precursor hydrolyses and polymerizes into a metal oxide network. Alternatively, the sol solution can be used to prepare thin films by dip coating. All as-made samples are transparent except for the samples derived from WO_3, which are dark blue. The as-made bulk samples or thin films were then calcined at 400 °C for 5 h in air to remove the surfactant species. Figure 1a shows typical X-ray diffraction (XRD) patterns for mesostructured zirconium oxides before and after calcination. The as-made zirconium inorganic/polymer mesostructure shows three diffraction peaks with lattice spacings $d = 115$, 65 and 59 Å. After calcination, the diffraction peaks appear at higher 2θ angles with $d = 106$, 60 and 53 Å. Both sets of diffraction peaks can be indexed as the (100), (110) and (200) reflections from two-dimensional hexagonal mesostructures with lattice constants $a = 132$ and 122 Å, respectively.

When $HO(CH_2CH_2O)_{106}(CH_2CH(CH_3)O)_{70}(CH_2CH_2O)_{106}H$ (abbreviated as $EO_{106}PO_{70}EO_{106}$) and $HO(CH_2CH_2O)_{75}(CH_2CH(CH_3CH_2)O)_{45}H$ (that is, $EO_{75}BO_{45}$) are used as the structure-directing agents under the above conditions, cubic mesophases are formed. Figure 1b shows the XRD patterns for the mesostructured TiO_2 formed using $EO_{75}BO_{45}$. The low-angle XRD pattern for the as-made samples shows six resolved peaks with d spacings of 100, 70, 58, 44, 41 and 25 Å. These peaks display d-value ratios of $\sqrt{2} : \sqrt{4} : \sqrt{6} : \sqrt{10} : \sqrt{12} : \sqrt{32}$, which are indexable as (110), (200), (211), (310), (222) and (440) reflections respectively, in the cubic $Im\bar{3}m$ space group. Following calcination of the sample at 400 °C, three XRD peaks are observed with d spacings of 76, 53 and 43 Å (ratios $\sqrt{2} : \sqrt{4} : \sqrt{6}$), which are similarly indexable as (110), (200) and (211) reflections of the cubic $Im\bar{3}m$ mesophase.

This synthetic procedure has been successfully applied to the preparation of mesoporous TiO_2, ZrO_2, Al_2O_3, Nb_2O_5, WO_3, HfO_2, SnO_2, and mixed oxides $SiAlO_{3.5}$, $SiTiO_4$, $ZrTiO_4$, Al_2TiO_5, ZrW_2O_8. Table 1 summarizes the d_{100} values measured for these different calcined oxides, along with other physical characteristics and material properties. All calcined samples show ordering lengths that are greater than 70 Å.

The appearance of low-angle diffraction peaks indicates that mesoscopic order is preserved in the calcined metal oxide materials. This is confirmed by transmission electron microscopy (TEM) images obtained from each of these samples. For example, Fig. 2a–f shows TEM images of mesoporous TiO_2, ZrO_2, Nb_2O_5 and $SiAlO_{3.5}$ recorded along the [110] and [001] zone axes of the mesostructures. In each case, well-ordered large channels are clearly observed to be arranged in hexagonal arrays. The pore/channel walls are continuous and have thicknesses of ~40–70 Å (Table 1). In addition, energy dispersive X-ray spectroscopy (EDX) measurements and quantitative elemental analysis made on each of the calcined samples show the expected primary metal element signals, along with very weak Cl signals, which confirm that the inorganic walls consist of predominantly metal–oxygen networks. Local EDX

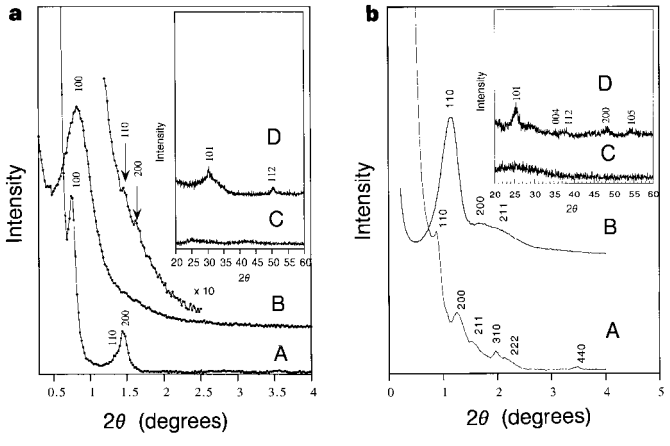

Figure 1 Powder X-ray diffraction patterns for mesoporous ZrO_2 (**a**) and TiO_2 (**b**). Traces A and C are low-angle and wide-angle XRD patterns of the as-made inorganic/$EO_{20}PO_{70}EO_{20}$ composite mesostructures, which have amorphous frameworks. Traces B and D are low-angle and wide-angle XRD patterns for the same mesoporous oxides calcined at 400 °C for 5 h in air. The high-angle diffractions are indexed according to their corresponding crystalline oxide phases. The XRD patterns were obtained with a Scintag PADX diffractometer using Cu Kα radiation.

composition analyses on mesoporous mixed oxides indicate that the different elements are distributed uniformly within the inorganic framework.

One advantage of the thick inorganic oxide walls is that domains of nanocrystallinity can be produced in the frameworks, while preserving the mesostructural integrities of the materials. For mesostructured materials with thinner framework walls, for example the M41S family of mesoporous solids, crystallization of inorganic species during the cooperative inorganic/organic assembly generally leads to macroscopic phase separation of the inorganic

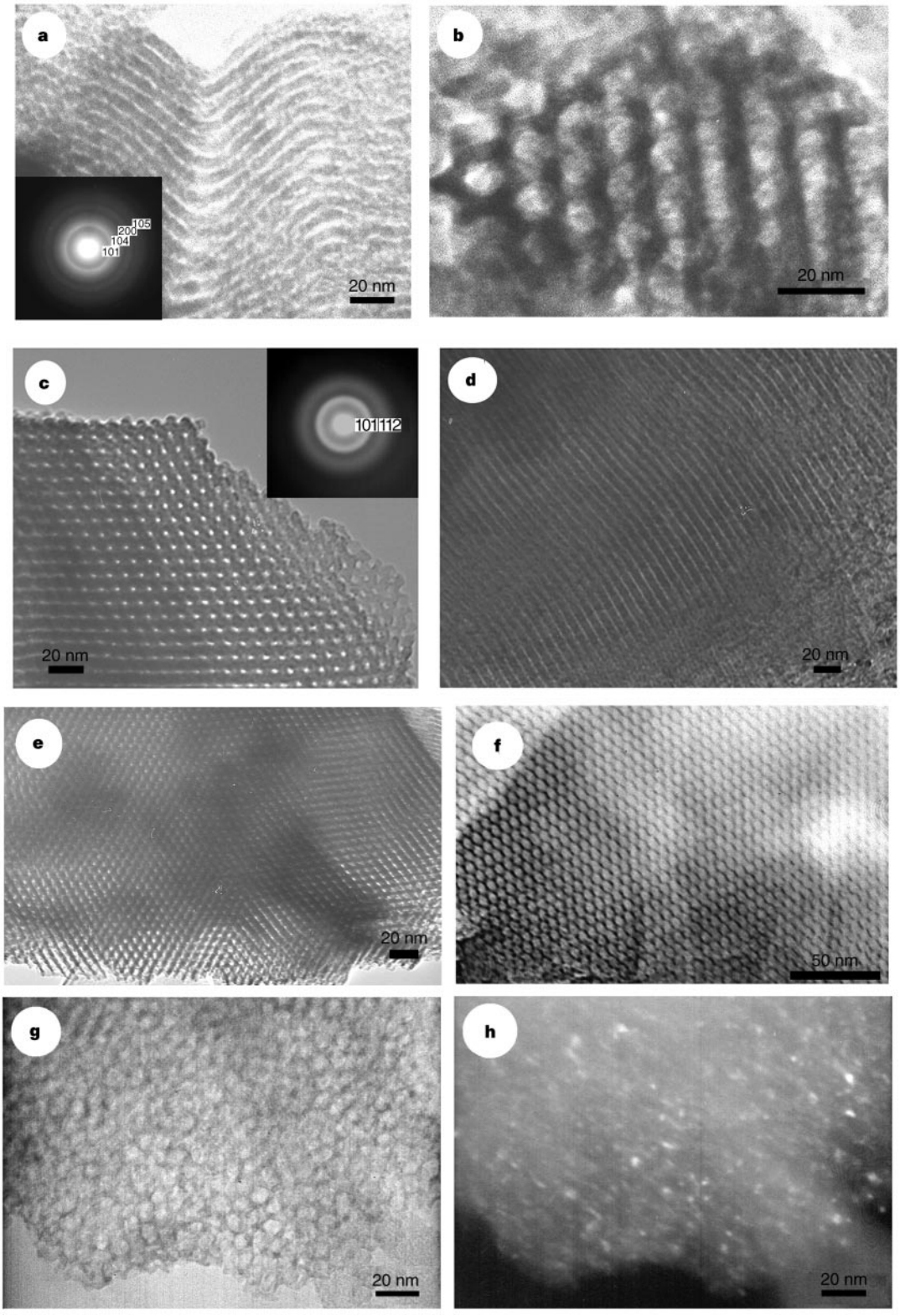

Figure 2 TEM images of mesoporous materials. Shown are TEM micrographs of two-dimensional hexagonal mesoporous TiO_2 (**a**, **b**), ZrO_2 (**c**, **d**), Nb_2O_5 (**e**) and $SiAlO_{3.5}$ (**f**). **a**, **d** Are recorded along the [110] zone axis and **b**, **c**, **e**, **f** along the [001] zone axis, respectively, of each material. Insets in **a** and **c** are selected-area electron diffraction patterns obtained on the image area. **g**, Bright-field TEM image of a thin slice of the mesoporous TiO_2 sample. **h**, Dark-field image obtained on the same area of the same TiO_2 sample. The bright spots in the image correspond to TiO_2 nanocrystals. The images were recorded with a 200 kV JEOL-2000 TEM. All samples were calcined at 400 °C for 5 h in air to remove the block copolymer surfactant species.

Table 1 Physicochemical properties of mesoporous metal oxides

Oxide	Inorganic precursor	d_{100}* (Å)	Wall structure	Wall thickness† (Å)	Nanocrystal size‡ (Å)	Pore size (Å)	BET surface area ($m^2 g^{-1}$)	BET surface area ($m^2 cm^{-3}$)	Porosity§	Physical properties
ZrO_2	$ZrCl_4$	106	Tetra. ZrO_2	65	15	58	150	884	0.43	Dielectric
TiO_2	$TiCl_4$	101	Anatase	51	24	65	205	867	0.46	Semiconductor
Nb_2O_5	$NbCl_5$	80	Nb_2O_5‖	40	<10	50	196	876	0.50	Dielectric
Ta_2O_5	$TaCl_5$	70	Ta_2O_5‖	40	<10	35	165	1,353	0.50	Dielectric
WO_3	WCl_6	95	WO_3	50	20	50	125	895	0.48	Semiconductor
SnO_2	$SnCl_4$	106	Cassiterite	50	30	68	180	1,251	0.52	Semiconductor $E_g = 4.05$ eV¶
HfO_2	$HfCl_4$	105	Amorphous	50	–	70	105	1,016	0.52	Dielectric
Al_2O_3	$AlCl_3$	186	Amorphous	35	–	140	300	1,188	0.61	Dielectric
SiO_2	$SiCl_4$	198	Amorphous	86	–	120	810	1,782	0.63	Dielectric
$SiAlO_{3.5}$	$SiCl_4/AlCl_3$	95	Amorphous	38	–	60	310	986	0.59	Dielectric
$Si_2AlO_{5.5}$	$SiCl_4/AlCl_3$	124	Amorphous	40	–	100	330	965	0.55	Dielectric
$SiTiO_4$	$SiCl_4/TiCl_4$	95	Amorphous	50	–	50	495	1,638	0.63	Dielectric
Al_2TiO_5	$AlCl_3/TiCl_4$	105	Amorphous	40	–	80	270	1,093	0.59	Dielectric
$ZrTiO_4$	$ZrCl_4/TiCl_4$	103	Amorphous	35	–	80	130	670	0.46	Dielectric
ZrW_2O_8	$ZrCl_4/TiCl_4$	100	Amorphous	45	–	50	170	1,144	0.51	NTE#

All samples were prepared using ethanol as a solvent, except HfO_2 where butanol was used. The structure-directing agent in all cases was $EO_{20}PO_{70}EO_{20}$ (see text). The aging process generally took 1–7 days.
* d-values of (100) reflection for samples calcined at 400 °C for 5 h in air.
† Thicknesses measured from TEM experiments. These values are consistent with the values estimated by subtracting the pore diameter from $2d_{100}/\sqrt{3}$.
‡ Nanocrystal sizes estimated from X-ray diffraction broadening using the Scherrer formula.
§ The porosity is estimated from the pore volume determined using the adsorption branch of the N_2 isotherm curve at the $P/P_0 = 0.983$ single point.
‖ Nucleation just started, extremely broad wide-angle diffraction.
¶ Direct allowed optical gap estimated from $(\alpha h\nu)^2 - h\nu$ plot of UV-vis absorption measurement, where α is the absorption coefficient.
# Materials with negative thermal expansion properties.

and organic components. This is because crystallization energies often dominate the interaction energies that stabilize the inorganic–organic interface, thereby disrupting the establishment of curved surfaces with three-dimensional mesostructural order[18,19]. This is particularly the case for non-lamellar phases[19,20]. In our approach, initial self-assembly of mesoscopically ordered as-synthesized materials with thick amorphous inorganic walls (no high-angle diffractions) provides a starting point from which nanocrystalline domains within the walls can nucleate. Relatively high densities of nanocrystallites can be produced within the thick framework walls, whose partially crystalline structure effectively sustains the local strain caused by the crystallization and prevents the mesostructure from collapsing.

X-ray diffraction studies on samples calcined at temperatures between 100 and 400 °C indicate that this crystallographic nucleation actually occurs during the calcination, but is limited to formation of nanocrystallite domains. Wide-angle X-ray diffraction studies of calcined mesoporous TiO_2, SnO_2, ZrO_2 and WO_3 samples clearly show broad peaks that can be indexed according to their corresponding crystalline oxide phases. For example, the traces 'D' in Fig. 1a and b insets show wide-angle diffraction patterns for the calcined ZrO_2 and TiO_2 samples. These data indicate that the inorganic framework may consist of nanocrystalline oxide domains. However, on the basis of this evidence alone, the possibility that these nanocrystallites are associated with phase separation cannot be strictly excluded[9,21].

An important technique to resolve this question and of particular value for the characterization of mesoscopically ordered semicrystalline inorganic frameworks is bright-field/dark-field TEM imaging, which has not previously[9,21] been used to substantiate claims of wall crystallinity in mesoporous materials. Selected-area electron diffraction patterns recorded on mesoporous TiO_2, SnO_2, ZrO_2 and WO_3 confirm that the walls of our materials are made up of nanocrystalline oxides that show characteristic diffuse electron diffraction rings (Fig. 2a and c insets). Figure 2g, h shows bright-field and dark-field TEM images recorded on the same area of a thin mesoporous TiO_2 sample. As can be seen in the dark-field image (Fig. 2h), the TiO_2 nanocrystals (~30 Å) are uniformly embedded in the continuous amorphous inorganic matrix to form semicrystalline wall structures. The nanocrystallite sizes are consistent with those estimated using the Scherrer formula from X-ray diffraction peak broadening (~10–30 Å, Table 1).

Calcination thus yields thermally stable ordered mesoporous solids with nanocrystalline domains in the inorganic oxide frameworks. N_2 adsorption/desorption isotherms showing similar type-IV curves[22] and porosities (~50%, Table 1) are obtained for the different calcined mesoporous oxides. Figure 3 shows N_2 adsorption and desorption isotherms that are representative of mesoporous TiO_2 and WO_3. Barrett–Joyner–Halenda (BJH) analyses show that the calcined TiO_2 and WO_3 exhibit pore sizes of 65 and 50 Å (Fig. 3 insets), respectively. The pore sizes (50–140 Å) of the mesoporous metal oxides listed in Table 1 are substantially larger than any of the non-silica mesoporous oxides previously reported[9–12]. Large hysteresis loops with shapes that are intermediate between typical H_1- and H_2-type[22] isotherms are observed for these mesoporous metal oxides. Such strong hysteresis is believed to be related to the capillary condensation associated with large pore channels[22] but may also be due to modulation of the channel structure.

Mesostructured inorganic/block copolymer composites for oxides of Ga, Ge, V, Zn, Cd, In, Sb, Mo, Re, Ru, Fe, Ni, Cr, Mn and Cu have also been synthesized using this block-copolymer/inorganic-salt methodology. The formation of large-pore mesoscopically ordered metal oxides with such simplicity and generality suggests that the same inorganic-oxide/block-copolymer assembly mechanisms may be operating. In fact, it is well-documented that alkylene oxide segments can form crown-ether-type complexes with many inorganic ions through weak coordination bonds[23]. After hydrolysis, the multivalent metal species (M) can associate preferentially with the hydrophilic poly(ethylene oxide) (PEO) moieties mediated by HCl, as indicated below.

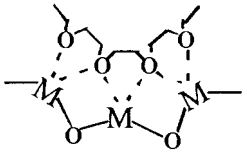

The resulting complexes then self-assemble according to the mesoscopic ordering directed principally by the microphase separation of the block copolymer species. Subsequent cross-linking and polymerization of the inorganic species occurs to form the mesoscopically ordered inorganic/block-copolymer composites. The use of the different relative hydrophobicities of PEO and poly(propylene oxide) has similarly been used to assemble mesostructured SiO_2 in an aqueous solution[8,24,25]. The proposed assembly mechanism for these diverse mesoporous metal oxides uses PEO–metal complexation interactions, in conjunction with (for example) electrostatic, hydrogen bonding, and van der Waals forces to direct mesostructure formation[1–5].

In addition, carrying out the assembly process in non-aqueous

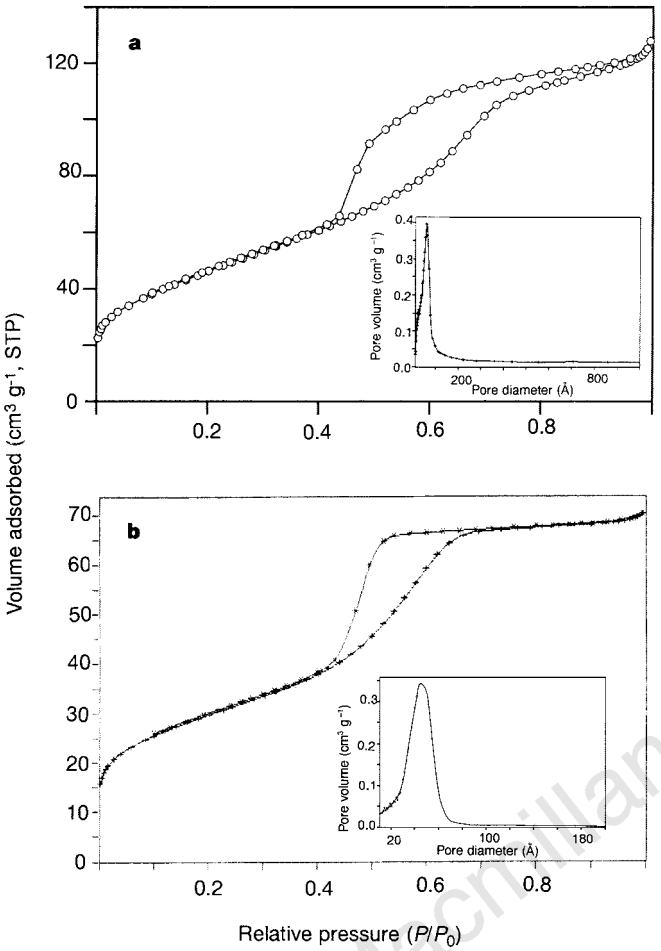

Figure 3 Nitrogen adsorption–desorption isotherms and pore-size distribution plots (insets) for calcined TiO_2 (**a**) and calcined WO_3 (**b**). Data were calculated using the BJH model from the adsorption branch isotherm. Both TiO_2 and WO_3 samples were calcined at 400 °C for 5 h in air. The isotherms were measured using a Micromeritics ASAP 2000 system. The samples were outgassed overnight at 200 °C before the analyses.

media using metal halides as the inorganic precursors effectively slows the hydrolysis/condensation rates of the metal species and hinders subsequent crystallization[26]. Restrained hydrolysis and condensation of the inorganic species appears to be important for forming mesophases of most of the non-silica oxides, because of their strong tendency to precipitate and crystallize into bulk oxide phases directly in aqueous media. Previous work on metal oxide mesostructure formation has been mostly carried out under aqueous conditions using reactive alkoxides as the inorganic precursors. Special processing, including for example the addition of stabilizing agents, is needed to slow the hydrolysis and condensation rates as demonstrated for TiO_2 (ref. 11). We have adopted a procedure that can regulate the hydrolysis/condensation and self-assembly processes simultaneously. We anticipate that with this method, the syntheses of other mesoscopically ordered inorganic compounds (including sulphides[16]) should also be possible. Such mesoporous materials with increasing richness of inorganic compositions have excellent potential for applications as high-surface-area battery electrodes, sensors, optoelectronic devices and catalysts. □

Received 16 April; accepted 24 August 1998.

1. Kresge, C. T., Leonowicz, M. E., Roth, W. J., Vartuli, J. C. & Beck, J. S. Ordered mesoporous molecular sieves synthesized by a liquid-crystal template mechanism. *Nature* **359,** 710–712 (1992).
2. Huo, Q. *et al.* Generalized synthesis of periodic surfactant/inorganic composite materials. *Nature* **368,** 317–321 (1994).
3. Huo, Q. *et al.* Organization of organic molecules with inorganic molecular species into nanocomposite biphase arrays. *Chem. Mater.* **6,** 1176–1191 (1994).
4. Tanev, P. T. & Pinnavaia, T. J. A neutral templating route to mesoporous molecular sieves. *Science* **267,** 865–868 (1995).
5. Antonelli, D. M. & Ying, J. Y. Synthesis and characterization of hexagonal packed mesoporous tantalum oxide molecular sieves. *Chem. Mater.* **8,** 874–881 (1996).
6. Förster, S. & Antonietti, M. Amphiphilic block copolymers in structure-controlled nanomaterial hybrids. *Adv. Mater.* **10,** 195–217 (1998).
7. Templin, M. *et al.* Organically modified aluminosilicate mesostructures from block copolymer phases. *Science* **278,** 1795–1798 (1997).
8. Zhao, D. *et al.* Triblock copolymer syntheses of mesoporous silica with periodic 50 to 300 angstrom pores. *Science* **279,** 548–552 (1998).
9. Tian, Z. *et al.* Manganese oxide mesoporous structures: mixed-valent semiconducting catalysts. *Science* **276,** 926–930 (1997).
10. Bagshaw, S. A. & Pinnavaia, T. J. Mesoporous alumina molecular sieves. *Angew. Chem. Int. Edn Engl.* **35,** 1102–1105 (1996).
11. Antonelli, D. M. & Ying, J. Y. Synthesis of hexagonal packed mesoporous TiO_2 by a modified sol-gel method. *Angew. Chem. Int. Edn Engl.* **34,** 2014–2017 (1995).
12. Ciesla, U., Schacht, S., Stucky, G. D., Unger, K. K. & Schüth, F. Formation of a porous zirconium oxo phosphate with a high surface area by a surfactant-assisted synthesis. *Angew. Chem. Int. Edn Engl.* **35,** 541–543 (1996).
13. Liu, P., Liu, J. & Sayari, A. Preparation of porous hafnium oxide in the presence of a cationic surfactant. *Chem. Commun.* 557–578 (1997).
14. Attard, G. S. *et al.* Mesoporous platinum films from lyotropic liquid crystalline phases. *Science* **278,** 838–840 (1997).
15. Ulagappan, N. & Rao, C. N. R. Mesoporous phases based on SnO_2 and TiO_2. *Chem. Commun.* 1685–1686 (1996).
16. Braun, P. V., Osenar, P. & Stupp, S. I. Semiconducting superlattices templated by molecular assemblies. *Nature* **380,** 325–328 (1996).
17. Sayari, A. & Liu, P. Non-silica mesostructured materials: recent progress. *Microporous Mater.* **12,** 149–177 (1997).
18. Stucky, G. D. *et al.* in *The Robert A. Welch Foundation 40th Conference on Chemical Research: Chemistry on the Nanometer Scale* 101–112 (Houston, Texas, 1996).
19. Monnier, A. *et al.* Cooperative formation of inorganic-organic interfaces in the synthesis of silicate mesostructures. *Science* **261,** 1299–1302 (1993).
20. Beck, J. S. *et al.* A new family of mesoporous molecular sieves prepared with liquid crystal templates. *J. Am. Chem. Soc.* **114,** 10834–10843 (1992).
21. Huang, Y., McCarthy, T. J. & Sachtler, W. M. Preparation and catalytic testing of mesoporous sulfated zirconium dioxide with partially tetragonal wall structure. *Appl. Catal. A* **148,** 135–154 (1996).
22. Gregg, S. J. & Sing, K. S. W. *Adsorption, Surface Area and Porosity* (Academic, London, 1982).
23. Bailey, F. E. Jr & Koleske, J. V. *Alkylene Oxides and their Polymers* (Marcel Dekker, New York, 1990).
24. Zhao, D. *et al.* Nonionic triblock and star diblock copolymer and oligomeric surfactant syntheses of highly ordered, hydrothermally stable, mesoporous silica structures. *J. Am. Chem. Soc.* **120,** 6024–6036 (1998).
25. Yang, P. *et al.* Triblock-copolymer-directed syntheses of large-pore mesoporous silica fibers. *Chem. Mater.* **10,** 2033–2036 (1998).
26. Vioux, A. Nonhydrolytic sol-gel routes to oxides. *Chem. Mater.* **9,** 2292–2299 (1997).

Acknowledgements. This work was supported by the NSF and the US Army Research Office. This work made use of MRL Central Facilities supported by the NSF. B.F.C. is a Camille and Henry Dreyfus teacher-scholar and an Alfred P. Sloan research fellow. We thank BASF (Mt Olive, New Jersey) and Dow Chemicals for providing block copolymer surfactants.

Correspondence and requests for materials should be addressed to G.D.S. (e-mail: stucky@chem.ucsb.edu).

Low interannual variability in recent oceanic uptake of atmospheric carbon dioxide

Kitack Lee*†, Rik Wanninkhof†, Taro Takahashi‡, Scott C. Doney§ & Richard A. Feely‖

** Rosenstiel School of Marine and Atmospheric Science/CIMAS, University of Miami, 4600 Rickenbacker Causeway, Miami, Florida 33149, USA*
† Atlantic Oceanographic and Meteorological Laboratory, NOAA, Miami, Florida 33149, USA
‡ Lamont-Doherty Earth Observatory of Columbia University, Palisades, New York 10964, USA
§ Climate and Global Dynamics, NCAR, Box 3000, Boulder, Colorado 80307, USA
‖ Pacific Marine Environmental Laboratory, NOAA, Seattle, Washington 98115, USA

An improved understanding of the partitioning of carbon between the atmosphere, terrestrial biosphere, and ocean allows for more accurate predictions of future atmospheric CO_2 concentrations under various fossil-fuel CO_2-emission scenarios. One of the more poorly quantified relevant processes is the interannual variability in the uptake of fossil-fuel CO_2 from the atmosphere by the terrestrial biosphere and ocean. Existing estimates, based on atmospheric measurements, indicate that